Science and Technology Indonesia
e-ISSN:2580-4391 *p*-ISSN:2580-4405
Vol. 11, No. 1, January 2026

Research Paper

The Synthesis of $CH_3NH_3PbI_{3-x}Br_x$ under Uncontrolled Humidity for Perovskite Solar Cell Application

Cahyorini Kusumawardani[1*], Jaslin Ikhsan[1], Kun Sri Budiasih[1], Herlambang Nugroho[1], Asri Widowati[2]

[1]*Department of Chemistry Education, Universitas Negeri Yogyakarta, Yogyakarta, 55281, Indonesia*
[2]*Department of Science Education, Universitas Negeri Yogyakarta, Yogyakarta, 55281, Indonesia*
*****Corresponding author**: cahyorini.k@uny.ac.id

Abstract

The $CH_3NH_3PbI_{3-x}Br_x$ have been successfully synthesized under uncontrolled humidity using two-step spin coating method continued by Ostwald ripening (OR) treatment. The incorporation of Br in the $CH_3NH_3PbI_3$ was done by diluting the previously formed of $CH_3NH_3PbI_3$ with various concentration of CH_3NH_3Br (MABr) solution. XRD analysis confirmed the formation of a tetragonal perovskite phase with reduced lattice parameters as the bromide concentration increased, indicating successful I^- to Br^- substitution. SEM and EDX characterization showed that moderate bromide incorporation (30-40 mg/mL) produced dense, uniform grains and homogeneous halide distribution, while excessive MABr led to non-uniform morphology and halide segregation, particularly under humid conditions. Optical analysis revealed a gradual blue shift in the absorption edge, consistent with band gap widening due to lattice contraction. The photovoltaic performance measurements demonstrated that higher MABr concentrations caused decreased current density and fill factor, resulting from excessive bromide content and defect formation. These findings showed that controlled bromide incorporation through Ostwald ripening with MABr concentration of 20 mg/mL effectively enhances the structural quality, film stability, and photovoltaic performance of $CH_3NH_3PbI_{3-x}Br_3$ perovskite solar cells under humid environments.

Keywords

Perovskite Solar Cells, $CH_3NH_3PbI_{3-x}Br_x$, Two-Step Spin Coating, Ostwald Ripening, Uncontrolled Humidity

Received: 6 October 2025, Accepted: 5 December 2025
https://doi.org/10.26554/sti.2026.11.1.298-310

1. INTRODUCTION

Perovskite-based solar cell (PSC) is one of the most potential third generation solar cells to replace silicon-based solar cells, because they have high efficiency and a simpler and cheaper fabrication process than the latter (Chen et al., 2015; Kojima et al., 2009; Wu et al., 2021). Perovskite, with a structure of ABX_3 ('A' and 'B' are various sizes of cations, while X is the anion) has electrical conductivity, and special optoelectronic properties that are easily tuned by adjusting the cations and/or the anion (Kurniawidi et al., 2025; Saptari et al., 2024). $CH_3NH_3PbX_3$ ('X' is halide, especially I) perovskites are so far being the most developed for solar cell application in the past ten years due to its high extinction coefficient (higher than 104 cm^{-1}), sharp absorption edge, and tunable electronic structure (Aftab et al., 2025; Wen et al., 2025). However, there is still need for improvement regarding the efficiency and stability of the solar cell for practical and commercial fabrication.

In PSC device, perovskite as the light absorber was deposited on electron transfer material layer (ETL) such as TiO_2, ZnO_2, SnO_2, ZrO_2, and while the perovskite active material is excited by energy photon higher than its bandgap, it will create exciton as the first step of electricity generation (Camizci et al., 2025; Wali et al., 2025). $CH_3NH_3PbI_3$ perovskite can be prepared through several techniques, such as one-step spin coating (Im et al., 2014; Yang et al., 2020; Zhang et al., 2017; Zhu et al., 2016), two-step deposition (Kim et al., 2024; Ngoc et al., 2024; Vidyasagar et al., 2018; Zhang et al., 2024), vapor-assisted solution technique (Li et al., 2025; Nguyen et al., 2023; Yang et al., 2020), and vacuum vapor deposition (Farooq et al., 2022). One-step spin coating method is the simplest and most widely used technique to prepare the $CH_3NH_3PbI_3$ on ETL for PSC application, but usually quite difficult to result a homogeny and less defect crystal according to the fast crystallization process (Kim et al., 2024). The high quality of perovskite film in one-step deposition method was then achieved by applying several modification techniques, such as using anti-solvent like chlorobenzene or toluene during the deposition process which need proper skill to apply to avoid problem of reproducibility (Jeon et al., 2014; Taylor et al., 2021; Zhang et al., 2025b).

The two-step method was then become a widely developed technique to synthesize the $CH_3NH_3PbI_3$, since it is easier to control the optoelectronic properties and morphology of the perovskite (Elangovan et al., 2024; Kusumawardani and Ikhsan, 2022; Zhang et al., 2024). The strategy to control PbI_2 layer and the deposition process are flexible and versatile, so it is easy to obtain the full coverage of PbI_2 layer which tends to improve the $CH_3NH_3PbI_3$ layer (Chen, 2017). The good reproducibility and high operability of the two-step method led to many following works in more modified technique undergoing to improve the quality of perovskite layer and enhance the solar cell performance (Kim et al., 2024; Sinelnik et al., 2024). It was reported that the complex processes involved during the perovskite formation could be achieved under specific atmosphere. Among some environmental parameters, moisture has become an important factor that influencing the $CH_3NH_3PbI_3$ formation, thus having impact to material properties and device efficiency and stability (Ogunniran and Martins, 2021). The relative humidity under ambient atmosphere is being detrimental factor toward the performance of solar cells, because the synthesis of $CH_3NH_3PbI_3$ in such high humidity resulted in a more non-uniform film consisting of crystal defect, crystallinity reduction of the film, and also optical properties decay (Wozny et al., 2015).

Thus, fabrication of $CH_3NH_3PbI_3$ must be performed under controlled humidity using instruments that provide specific synthesis parameters, which is a problem in some general laboratories with limitations. The incorporation of small Br to substitute I -$CH_3NH_3PbI_{3\text{-}x}Br_x$- have been successfully improved the efficiency and the stability of perovskite solar cells, because the infiltration of Br resulted in larger grain with less pinhole (Yang et al., 2016). Several research reported the synthesis applying the Ostwald ripening process under ambient air and the influences toward the $CH_3NH_3PbI_{3\text{-}x}Br_x$ perovskites properties and the solar cell performance. But there is no exact or optimum I^- amount replaced by Br^- in a specific humidity reported in the previous research. In this article, we developed the facile synthesis of $CH_3NH_3PbI_{3\text{-}x}Br_x$ under tropical ambient humidity (over humid conditions) through two-step spin coating (Chen et al., 2022; Ogunniran and Martins, 2021; You et al., 2014). To avoid the detrimental effect of the uncontrolled humidity, we conduct a post-treatment to the resulted perovskite material by dissolving the formed $CH_3NH_3PbI_3$ thin film into CH_3NH_3Br containing solution (Ostwald ripening process) to enlarge the crystal size with less defect. The concentration of CH_3NH_3Br was varied to study its influence on the conversion mechanism of unformed PbI_2 to the $CH_3NH_3PbI_{3\text{-}x}Br_x$ perovskite material, the properties of $CH_3NH_3PbI_{3\text{-}x}Br_x$ material and the performance of perovskite solar cells based on synthesized $CH_3NH_3PbI_{3\text{-}x}Br_x$ material.

2. EXPERIMENTAL SECTION

2.1 Materials

The main materials used in this research are PbI_2 (Merck), CH_3NH_3I (Great Solar), CH_3NH_3Br (Great Solar), Dimethyl Formamide (Flucka), Absolute Isopropanol (Merck), FTO glass substrate (Great Solar), Pt counter electrode (Great Solar), and Spiro-O-MeTAD (Great Solar). All materials were used without further purification.

2.2 Methods

Thin films preparation: TiO_2 paste made from TTIP in ethanol (1:10 (V/V)) was coated to FTO glass substrate under spinning at 3000 rpm for 40 s and annealed at 500 °C for 30 minutes to result a blocking layer (c-TiO_2). The mesoporous titanium dioxide (m-TiO_2) was synthesized following previous developed procedure Cahyorini et al. (2012) with slight modification. The electron transporting layer (ETL) was form on previous FTO/c-TiO_2 by adding the m-TiO_2 paste in ethanol (2/5 (w/w)) film at 3000 rpm for 40 s and calcined at 500 °C for 30 minutes.

Synthesis of $CH_3NH_3PbI_{3\text{-}x}Br_x$ through two step deposition method: First, the $CH_3NH_3PbI_3$ as an active layer was deposited of previous FTO/c-TiO_2/m-TiO_2 thin film through two-step coating method. A 1 M of PbI_2 (DMF) was spin coated on the film at 4000 rpm for 30 s and dried on the hot plate at 150 °C for 30 minutes. The conversion of PbI_2 to perovskite material was done by adding various concentration of CH_3NH_3I (MAI) containing solution (in isopropanol) under spinning at 4000 rpm for 30 s. The resulting film were dried on the hot plate at 150 °C for 30 minutes to complete the formation of $CH_3NH_3PbI_3$ (Kusumawardani and Ikhsan, 2022). The Ostwald ripening post-treatment was performed to the TiO_2/$CH_3NH_3PbI_3$ film by adding the film with various concentration of CH_3NH_3Br (MABr) in isopropanol (20–50 mg/mL) under spinning at 4000 rpm for 30 s to prepare $CH_3NH_3PbI_{3\text{-}x}Br_x$. As comparison, the Ostwald ripening process was also done using MAI at optimum concentration result in $CH_3NH_3PbI_3$. All the synthesis processes were performed under over humid conditions (humidity of 70-80%). The nitrogen gas was applied to the thin film during the synthesis to minimize the high humidity effect.

Fabrication of perovskite solar cells: Perovskite solar cells are constructed by FTO (15 Ω, 2 mm thick) substrate glass coated with TiO_2/perovskite as photoanode and FTO (15 Ω, 2 mm thick) coated silver as photocathode. Spiro-O-MeTAD was used as electrolyte and spin coated on the surface of photoanode. The two glass substrate electrodes are joined and interposed with a thermoplastic sealant film spacer (~50μm thick) to avoid short circuiting.

Characterization: the resulted materials before and after the Ostwald ripening process were characterized using XRD (Rigaku 1000) to characterize the crystallinity, UV-Vis Spectrophotometer (UV-2600, Shimadzu) to observe the absorption of the materials, and SEM (Hitachi) to study the material's morphology. The solar cell performance measurement: current-voltage density curves were measured using a Kethley 2200 instrument, with a solar simulator (10500 Abet Tech.) emitted under 1.5 AM conditions and producing a beam intensity of 100 mW/cm^2. The current-voltage density was measured over an area of 1 cm × 1 cm under conditions with illumination.

3. RESULT AND DISCUSSIONS

3.1 The $CH_3NH_3PbI_3$ Perovskite Synthesized Through Two-Step Deposition

The $CH_3NH_3PbI_3$ perovskite has been successfully synthesized on the surface of TiO_2 thin film through two-step deposition method under ambient high humidity. To study the structure of resulting perovskite, the synthesized films were analyzed using XRD and the results are shown in Figure 1. The conversion efficiency of PbI_2 to form the perovskite, the diffractogram of resulted $CH_3NH_3PbI_3$ were compared with XRD pattern of PbI_2 seed layer over titania films. The sharp main peaks on 14.3°, 23.6° and 28.8° confirmed the appearance of $CH_3NH_3PbI_3$ on the films prepared at MAI concentration of 20 and 40 mg/mL, which correspond to (110), (211), and (220) planes (Aftab et al., 2025; Jeon et al., 2014; Kim et al., 2022). The broader peaks at the same range were also found in the films prepared at MAI concentration of 50 mg/mL, indicated the low crystallinity of the perovskite and the initial precursors. The PbI_2 peaks characteristic at around 12.7° and 25.6° (Watthage et al., 2016) and MAI peaks at ~20°, 29°, and 33.5° were still found in the films prepared at all MAI concentrations, which are regarded as incomplete reaction. The characteristics of TiO_2 peaks at 25° and 33.5° were also found in the XRD results, indicated that the $CH_3NH_3PbI_3$ on the TiO_2 surface is not completely covering the TiO_2.

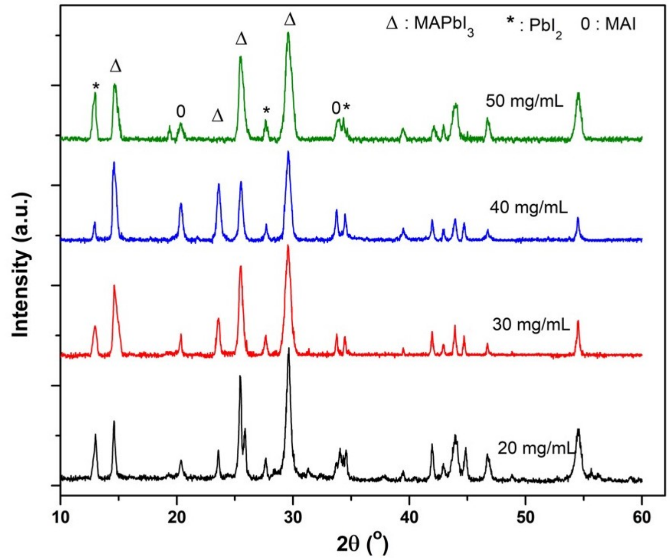

Figure 1. XRD Difractogram of Perovskite Synthesized by Two-Step Method at Various Concentration of MAI

The XRD analysis revealed that the higher concentration of MAI (up to 40 mg/mL) in the second-spin coating step led to the lower unformed PbI_2 on the TiO_2 surface. This result was similar as reported in most research on synthesis of perovskite using spin coating method both in one or two step (Cheng and Ding, 2021). However, the sharper peaks of perovskite material can be obtained using lower precursor concentrations (at around 20-25 mg/mL) while the synthesis performed under controlled temperature and humidity (Liu et al., 2020b). However, the $CH_3NH_3PbI_3$ have been successfully synthesized under ambient conditions without sophisticated facilities resulting in perovskite materials with moderate crystallinity. The particle of the perovskites was determined using Scherrer formula based on main peaks of XRD diffractograms, and the results were listed in Table 1. It was revealed that there is no specific trend in particle size relating to the change of MAI concentration, except that the highest particle size resulted from the synthesis with 20 mg/mL MAI, even the crystallinity is quite low with high peak of unformed PbI_2.

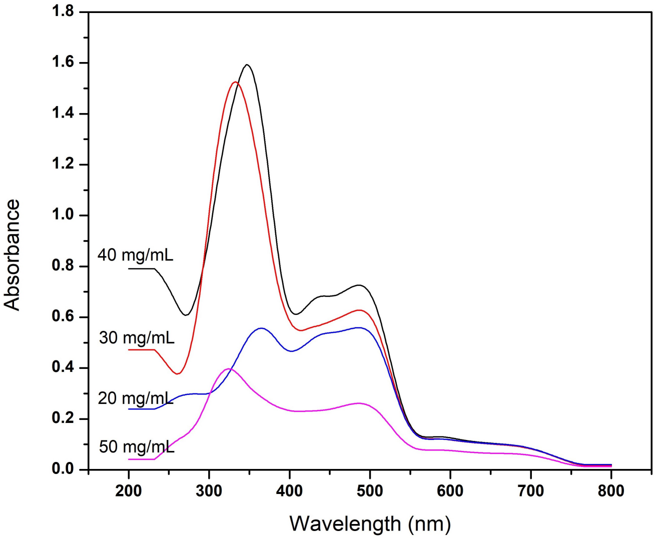

Figure 2. UV/Vis Analysis Results of Perovskite Synthesized by Two-Step Method at Various Concentration of MAI

The XRD data were then refined using Rietica v4.2 software to determine the lattice parameter, crystal texture and orientation and the data listed at Table 2. The refined tetragonal lattice parameters (a and c) remain within a narrow range of approximately 8.84-8.88 Å and 12.60-12.70 Å, indicating that all samples preserve the characteristic tetragonal phase of $CH_3NH_3PbI_3$ without significant lattice distortion. A slight contraction in the c-axis and stabilization of the a-parameter with increasing MAI concentration suggests improved crystal packing and reduced lattice strain at higher precursor ratios. The I_{110}/I_{220} area ratio increases progressively from 20 mg to 40 mg, indicating enhanced (110) texture with rising MAI concentration, and then decreases slightly at 50 mg, suggesting a minor relaxation of the preferred orientation at higher precursor loading. The orientation analysis-evaluated through the texture coefficient (TC) shows a distinct trend of enhanced preferential orientation along the (110) planes up to an optimal concentration (≈40 mg), followed by a minor reduction at

Table 1. Particle Size of Perovskites Synthesized at Various Concentration of MAI Based on XRD Analysis

Angle	hkl	Perovskite Particle Size (±10 nm)			
		20 MAI	30 MAI	40 MAI	50 MAI
14.3	110	118	76	99	88
23.6	211	180	114	144	138
28.8	220	193	128	160	142

Table 2. Refines Lattice Parameter, Crystal Orientation, and Texture Coefficient of $CH_3NH_3PbI_3$ at Various MAI Concentration

	MAI Concentration (mg/mL)			
	20	30	40	50
Crystal phase	tetragonal	tetragonal	tetragonal	tetragonal
a (Å)	8.8453	8.8769	8.8775	8.8635
c (Å)	12.6541	12.6140	12.5633	12.6551
I_{110}/I_{220}	0.8671	1.2095	1.8415	1.2718
TC_{110}	0.0279	0.0178	0.0127	0.0291

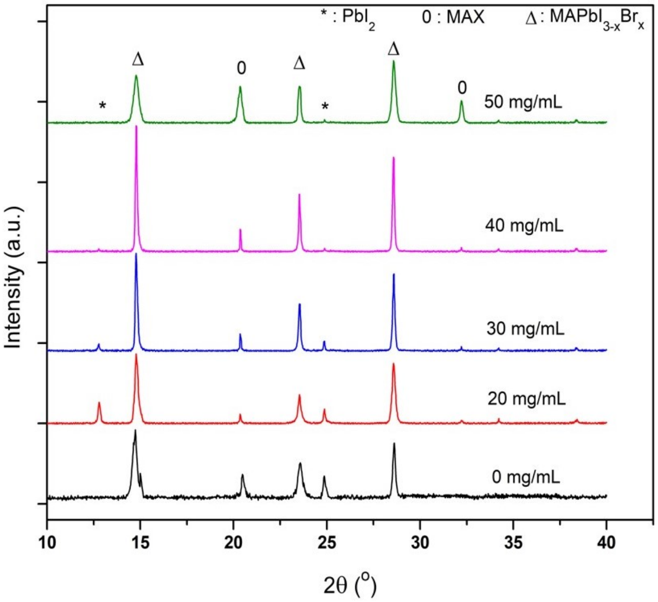

Figure 3. X-Ray Difractogram of Perovskite After Ostwald Ripening Treatment with Various Concentration of MABr

Table 3. Bandgap Energy (E_g) Synthesized at Various Concentration of MAI

MAI Concentration (mg/mL)	E_g (eV)
20	2.07
30	2.12
40	2.16
50	2.03

higher loading.

The structural evolution on MAI variation from 20 to 50 mg/mL closely aligns with previous reported research which demonstrated that an excess of MAI lead to the surface defect passivation, enhancing crystallinity, and promoting the preferential crystal growth along (110) and (220) planes to improve carrier transport and reducing recombination (Kim et al., 2024). The controlled MAI concentration also results in grain connectivity enhancement and lattice strain reduction indicated by narrow a-c variation, consistent with previous research (Elangovan et al., 2024). In contrast, a different result reported that excessive MAI content inducing PbI_2 deficiency and organic residue formation led to decline crystallinity and orientation homogeneity (Ahn et al., 2016). The present results in accordance with these findings that the 40 mg/mL MAI provides the most favorable balance between lattice stability and preferred orientation on (110) planes as theoretically advantageous for improved charge transfer and solar cell device based on $CH_3NH_3PbI_3$.

The optical properties of resulted perovskite were analyzed using UV/Vis Spectrophotometer and the analysis results are shown in Figure 2 which indicated that the absorption came from every separate component in the thin films. Absorption of UV-Vis light results in electron transition, which promotes electrons from a lower energy of ground state orbital to a high energy of excited state orbital. $CH_3NH_3PbI_3$ material prepared at various CH_3NH_3I concentrations have shown electronic transitions of $\pi \rightarrow \pi^*$ (absorption range of 200-400 nm) and nπ $\rightarrow$ π^* (absorption range of 500–700 nm) transition types (Catalán and Catalán, 2011; Sutrisno et al., 2018). The high intensity of n$\rightarrow\pi*$ transition indicated that the prepared perovksite material is highly active in visible area (Sugiyarto et al., 2018; Xing et al., 2013). Among synthesis results at various concentrations of CH_3NH_3I, perovskite films prepared at 30 and 40 mg/mL are comparable high. The high amount

Table 4. Particle Size of the Perovskites After Ostwald Ripening Treatment with Various Concentration of MABr Based on XRD

		Perovskite Particle Size (±14 nm)				
Angle	hkl	40 MAI	20 MABr	30 MABr	40 MABr	50 MABr
14.3	110	168	204	226	238	172
23.6	211	240	296	332	335	244
28.8	220	265	322	346	362	253

Table 5. Refines Lattice Parameter, Crystal Orientation, and Texture Coefficient of $CH_3NH_3PbI_{3-x}Br_x$ at Various MABr Concentration

Crystal Phase	MAX Concentration (mg/mL)				
	40 MAI	20 MABr	30 MABr	40 MABr	50 MABr
tetragonal	tetragonal	tetragonal	tetragonal	tetragonal	tetragonal
a (Å)	8.7991	8.6396	8.6283	8.6259	8.6237
c (Å)	12.6538	12.6171	12.5887	12.5242	12.6042
I_{110}/I_{220}	1.8561	1.3384	1.2831	1.1176	0.7924
TC_{110}	1.0000	0.9240	1.4070	1.8110	0.6940

of unformed PbI_2 in the film prepared at CH_3NH_3I concentration of 20 mg/mL resulted in a lower absorption intensity. The lowest absorption intensity of the film prepared at CH_3NH_3I concentration of 50 mg/mL was caused by the high unformed of precursor materials.

Further analysis of UV/Vis spectrum was done to obtain band gap energy of the prepared thin films using Tauc formula and the results listed in Table 3. It showed that the band gap energy increased with the increasing of MAI concentration up to 40 mg/mL and decline with the MAI concentration of 50 mg/mL. Thus, considering the better crystallinity of the film prepared at 40 mg/mL than at 30 mg/mL and the moderate band gap energy of perovskites prepared with 40 mg/mL MAI, the next step of Ostwald ripening process to prepare the $CH_3NH_3PbI_3$ were performed to the film synthesized with CH_3NH_3I concentration of 40 mg/mL.

3.2 Result of Ostwald Ripening Post-Treatment using CH_3NH_3Br

The Ostwald ripening (OR) treatment was applied to the currently synthesized of TiO_2/ $CH_3NH_3PbI_3$ to convert the unformed precursors become a high crystallinity of $CH_3NH_3PbI_{3-x}Br_x$. The XRD diffractogram results (Figure 3) showed that OR is successfully being a dominant step to synthesize the perovskite. In the OR process, the small crystal of $CH_3NH_3PbI_3$ dissolved in the CH_3NH_3Br solution and formed a larger crystal. At the CH_3NH_3Br concentration of 20 mg/mL, OR treatment becomes the dominant reaction of the $CH_3NH_3PbI_3$ formation with the disappearance of unformed precursor peaks, even there are still PbI_2 peaks left. When the CH_3NH_3Br concentration was increased to 30 and 40 mg/mL, the PbI_2 peaks characterization disappeared and perovskite became the dominant phase, which means all PbI_2 have already converted to perovskite. The higher CH_3NH_3Br concentration decreases the total Gibbs free energy which lead to the increase of dense and homogenous $CH_3NH_3PbI_{3-x}Br_x$ formation. However, the high CH_3NH_3Br concentration tends to be the perovskite agglomeration layer due to the low intensity of the main perovskite peaks. Further increased of CH_3NH_3Br concentration (>40 mg/mL) resulted in an lower crystallinity layer since all PbI_2 seed have been converted and the excess of CH_3NH_3Br might form the blocking layer above the perovskite as also reported by (Yang et al., 2016). The high humidity also contributes to the perovskite particle agglomeration, where the water vapor would moisture the crystal through methyl as hydrophobic site (Ogunniran and Martins, 2021).

The particle size of the perovskite was determined based on XRD spectra, and the results were listed in Table 4, which showed that the Ostwald ripening treatment successfully dissolved the unformed precursors and small previously synthesized perovskites using two-step methods to result a higher crystal size with much better crystallinity. In addition, the incorporation of Br into the perovskite crystal even led to a much higher crystal size and crystallinity. The existence of Br facilitates the fast dilution of previously formed perovskite and unformed precursors and lead to the arrangement and self-assembly the perovskite crystal (Yang et al., 2016). But there is an optimum concentration of the MABr for the OR treatment, since a high concentration of MABr resulted in a layer that blocks the dilution of the previously formed perovskite materials and the diffusion of amine groups to achieve the unformed PbI_2 seeds. This result was in accordance with the research reported by Kim et al. (2016), which showed that the Ostwald ripening treatment successfully dissolved the unformed precursors and small previously synthesized perovskites using

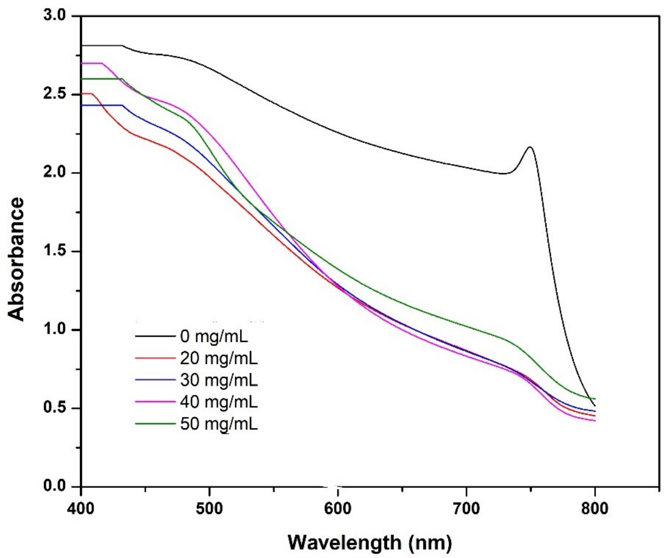

Figure 4. UV/Vis Absorbance Spectrum of Perovskite After Ostwald Ripening Treatment with Various Concentration of MABr

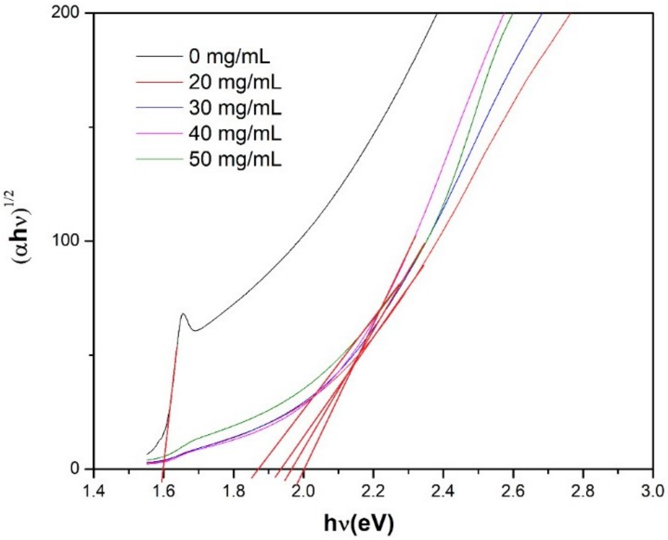

Figure 5. Band Gap Energy of Perovskite After Ostwald Ripening Treatment with Various Concentration of MABr

two-step methods to result a higher crystal size with much better crystallinity.

The XRD patterns of $CH_3NH_3PbI_{3\text{-}x}Br_x$ thin films treated with varying MABr concentrations through Ostwald ripening post-treatment confirmed a stable tetragonal perovskite phase as determined from the refinement data using Le Bail under Rietiva v4.2 (Table 5). Both lattice parameters a and c decreased from 8.7991 Å and 12.6538 Å (0 MABr or 40 mg/mL MAI) to 8.6259 Å and 12.5242 Å with 40 mg/mL MABr, indicating contraction of crystal lattice due to partial substitution of iodide with smaller anion. At excessive MABr (50 mg/mL), a slight increase in c suggested strain relaxation or halide segregation. The similar trend with the results before the OR post-treatment, the preferred orientation analysis showed a dominant (110) texture at moderate MABr levels (TC_{110} = 1.41-1.81), while higher concentration reduced (110) orientation (TC_{110} = 0.69), implying reorientation and increased polycrystallinity. Thus, Br incorporation promotes lattice shrinkage and texture optimization up to ~40 mg/mL, consistent with reported mixed-halide perovskite behavior (Jeon et al., 2014).

The OR post-treatment also highly influences the optical properties of the perovskites as absorption edges shifted from around 600 nm to about 800 nm at all CH_3NH_3Br concentration with a similar trend of the spectra (Figure 4). The dominant phase of perovskites provides a higher activity of the films in the visible area, as also reported by many researchers (Al-janabi et al., 2025; Kim et al., 2024; Ming et al., 2024; Zhang et al., 2025a). The more homogenous perovskites crystal with high particle size, means by the less crystal defect and pinholes lead to a higher intensity of visible light absorption (Yang et al., 2016). The Tauc graphs (Figure 5) showed the contrast trend to the previous step that the increasing concentration of MABr up to 40 mg/mL (2 eV) lead to the lower redshift of the perovskites gap energy (1.84 eV at 20 mg/mL MABr) and the highest redshift provided by the MABr concentration of 50 mg/mL. The perovskite thin film with 0 mg/mL MABr was prepared by OR post treatment using 40 mg/mL MAI to form $CH_3NH_3PbI_3$ resulted in a band gap energy of 1.6 eV. Similar phenomena were reported by Yilmaz and Yerci that found the band gap energy of $CH_3NH_3PbI_{3\text{-}x}Br_x$ was 1.55 eV at x=0 and raised with the increased of x (Eg = 2.30 eV at x=3) (Yilmaz and Yerci, 2019).

The increase in observed band gap energy with higher MABr concentration after OR treatment is attributed to Br substitution in the perovskite lattice. Since iodide with higher ionic radius replaced by bromide, it induces lattice contraction and change the overlapping orbital between Pb and halide and lead to a wider energy gap between orbital 5p of halide (valence band) and orbital 6p of Pb (conduction band) (Mehra et al., 2024). As a consequent, the optical band gap increases, and provides a lower redshift of the absorption edge. Furthermore, at higher bromide concentrations, the Ostwald ripening process promotes improved crystallinity and reduced defect density, which diminished localized states within the band gap and enhanced the precision of optical transitions (Yang et al., 2016). This compositional tuning mechanism enables band gap modulation from approximately 1.6 eV for $CH_3NH_3PbI_3$ to about 2.2 eV for $CH_3NH_3PbBr_3$, consistent with previous reports on mixed-halide perovskites (Guo et al., 2025; Sa et al., 2022). However, the excessive MABr concentration (50 mg/mL) causes halide segregation, defect formation, and structural relaxation, which lead to redshifted absorption and reduced band gap.

The surface morphology of $CH_3NH_3PbI_{3\text{-}x}Br_x$ films prepared via Ostwald ripening with varying MABr concentra-

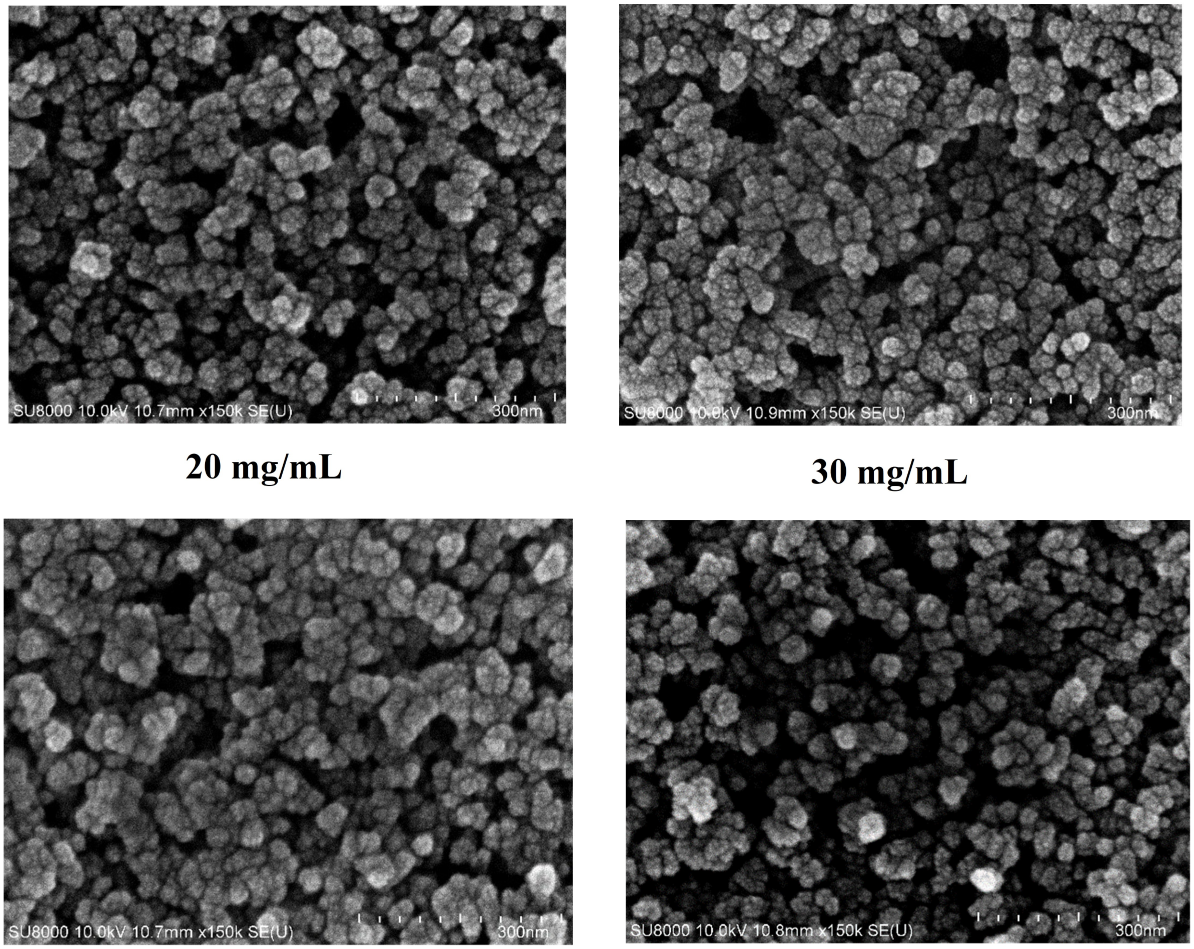

20 mg/mL

30 mg/mL

40 mg/mL

50 mg/mL

Figure 6. UV/Vis Spectra of Perovskite After Ostwald Ripening Treatment at Concentration of MBr

tions was studied from SEM micrographs in Figure 6. At 20 mg/mL, the perovskite film exhibits relatively small and irregular grains with noticeable voids, suggesting incomplete crystal coalescence. Increasing the MABr concentration to 30 and 40 mg/mL results in larger, more compact grains with reduced grain boundaries, indicating enhanced crystal growth and improved film uniformity due to optimized halide diffusion during ripening (Jeon et al., 2014; Zhou et al., 2015). The existence of pinholes in the perovskite layer indicated the quality of $CH_3NH_3PbI_{3-x}Br_x$ thin film even after applying the Ostwald ripening process, which highly related to the uncontrolled humidity. Wozny et al. (2015) reported the influence of humidity in the synthesis of formamidium lead-triiodide perovskite, the higher humidity resulted in a more non-homogenous film consisting of many pinholes, a film crystallinity reduction, and a decay on optical properties. However, at 50 mg/mL, partial grain coarsening and non-uniform morphology appear, likely caused by excessive bromide content that disrupts balanced nucleation and growth. These morphological improvements at moderate MABr concentrations correlate with the observed enhancement in crystal orientation and reduced trap-assisted recombination in the films.

The EDX spectra (Figure 7) confirm the presence of constituent elements (C, N, O, Ti, Br, Sn, and Pb) corresponding to the $CH_3NH_3PbI_{3-x}Br_x$ perovskite films synthesized at 20 and 40 mg/mL MABr. Both samples exhibit strong peaks of Pb and I, along with clear Br signals, verifying successful incorporation of bromide into the perovskite lattice. Compared with the 20 mg/mL film, the 40 mg/mL sample shows a significantly higher Br content (6.68 wt% vs 0.19 wt%) and a corresponding reduction in I intensity, confirming progressive $I^- \rightarrow Br^-$ substitution during Ostwald ripening. The Ti and Sn peaks originate from the underlying TiO_2 compact/mesoporous layers and FTO substrate, while the low C and N levels correspond to methylammonium organic group. The increase in Br fraction at 40 mg/mL suggests enhanced halide diffusion and lattice modification, consistent with the observed lattice contraction in XRD and the optical band gap widening associated with

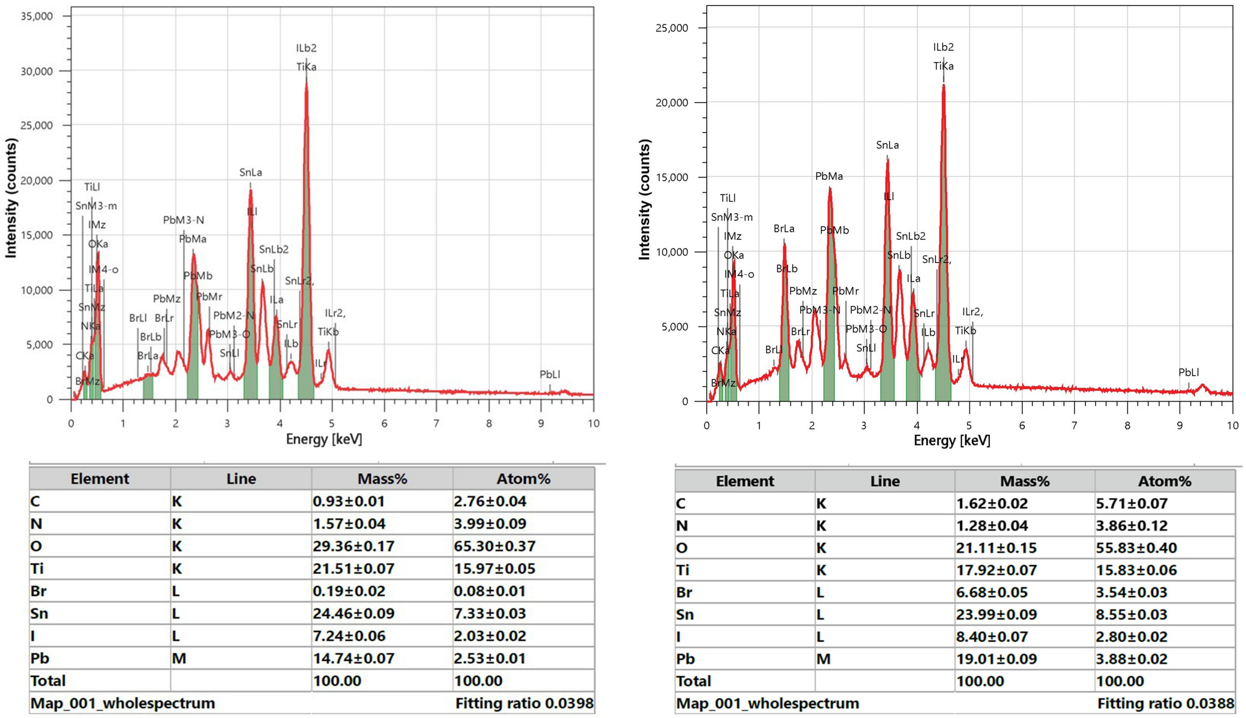

Element	Line	Mass%	Atom%
C	K	0.93±0.01	2.76±0.04
N	K	1.57±0.04	3.99±0.09
O	K	29.36±0.17	65.30±0.37
Ti	K	21.51±0.07	15.97±0.05
Br	L	0.19±0.02	0.08±0.01
Sn	L	24.46±0.09	7.33±0.03
I	L	7.24±0.06	2.03±0.02
Pb	M	14.74±0.07	2.53±0.01
Total		100.00	100.00
Map_001_wholespectrum			Fitting ratio 0.0398

Element	Line	Mass%	Atom%
C	K	1.62±0.02	5.71±0.07
N	K	1.28±0.04	3.86±0.12
O	K	21.11±0.15	55.83±0.40
Ti	K	17.92±0.07	15.83±0.06
Br	L	6.68±0.05	3.54±0.03
Sn	L	23.99±0.09	8.55±0.03
I	L	8.40±0.07	2.80±0.02
Pb	M	19.01±0.09	3.88±0.02
Total		100.00	100.00
Map_001_wholespectrum			Fitting ratio 0.0388

Figure 7. EDX Graph and Surface Elemental Analysis of $CH_3NH_3PbI_{3-x}Br_x$ Synthesized at 20 (left) and 40 mg/mL (Right) MABr

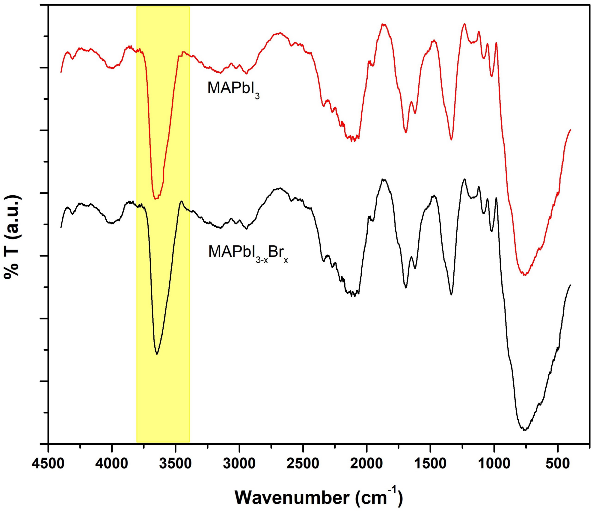

Figure 8. EDX FTIR Spectra of $CH_3NH_3PbI_3$ (Red) and $CH_3NH_3PbI_{3-x}Br_x$ Synthesized at 40 mg/mL MABr (Black)

higher bromide incorporation. Both SEM and EDX analysis results indicate that humidity strongly influences the surface morphology and halide composition of $CH_3NH_3PbI_{3-x}Br_x$ films during Ostwald ripening. Under over-humid conditions, moisture can partially dissolve the perovskite layer and promote ion migration, leading to non-uniform nucleation and recrystallization (Chen et al., 2022; Ogunniran and Martins, 2021; You et al., 2014). Overall, moderate bromide addition improves both structural stability and environmental tolerance against humidity-induced degradation.

The FTIR spectra of $CH_3NH_3PbI_3$ and $CH_3NH_3PbI_{3-x}Br_x$ (40 mg/mL MABr) (Figure 8) both exhibit the expected C–H and N–H vibrations of the methylammonium cation, confirming that the organic A-site remains intact. However, the Br-substituted film shows a noticeably stronger broad absorption between ~3200-3600 cm^{-1}, indicating enhanced hydrogen-bonding or increased surface hydroxyl/adsorbed-water species, which may reflect greater surface polarity or residual organics. In the low-frequency region, the Pb–X lattice vibrations shift to higher wavenumbers in the mixed-halide film, consistent with the formation of shorter, stiffer Pb–Br bonds. This spectral shift aligns with previous observations that halide substitution contracts the perovskite lattice and increases bandgap (e.g., through changed Pb–X bonding) in mixed halide perovskites. However, subtle differences are observed in the $MAPbI_3$ spectrum which exhibits sharper and more intense peaks compared to $CH_3NH_3PbI_{3-x}Br_x$.This peak broadening in the mixed halide perovskite suggests increased structural disorder arising from the mixed halide occupation and a distribution of local environments surrounding the MA$^+$ cations (Fykouras et al., 2023; Huang et al., 2024). These results demonstrate that bromide incorporation primarily affects the inorganic $[PbX_6]^{4-}$ octahedral framework rather than the organic component, with the

Table 6. Device Performance of Perovskite Solar Cell

Solar Cell System	I_{sc} (mA/cm^2)	V_{oc} (V)	FF (%)	PCE (%)
20 mg/mL MABr	21.38	0.99	60.95	12.56 ± 0.04
30 mg/mL MABr	20.76	0.98	54.97	11.64 ± 0.03
40 mg/mL MABr	19.42	0.97	45.03	8.66 ± 0.05
50 mg/mL MABr	15.94	0.98	41.42	4.27 ± 0.07

subtle spectral changes reflecting modified hydrogen bonding interactions between the MA$^+$ cations and the mixed halide lattice without fundamentally altering the perovskite structure (Gan et al., 2019; Verma and Jain, 2024).

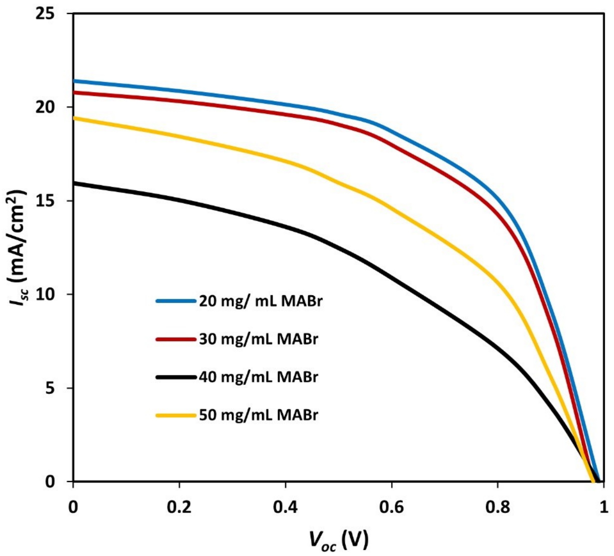

Figure 9. I-V of Perovskite Solar Cells at Variation Concentration of MABr

3.3 The Perovskite Solar Cells based on $CH_3NH_3PbI_{3\text{-}x}Br_x$

The resulting perovskite materials were then applied in the perovskite solar cells, and the performance of the PSCs was measured as short-circuit current density (I_{sc}) and open circuit voltage (V_{oc}) under standard global (AM 1.5 solar irradiation) and the results showed in Figure 9. From the I_{sc} vs V_{oc} curve, the fill factor (FF) of the solar cell can be determined by the following Equation 1.

$$FF = \frac{V_{\max} I_{\max}}{V_{oc} I_{sc}} \tag{1}$$

where $V_{\max}$ and $I_{\max}$ are the voltage and current at the maximum power point of the I-V curve. The overall performance conversion efficiency (PCE) of the solar cell determined using Equation 2.

$$\text{PCE} = \frac{V_{oc} I_{sc} FF}{P_{\text{in}}} \times 100\% \tag{2}$$

where P_{in} is the incident power irradiance. The photovoltaic parameters of $CH_3NH_3PbI_{3-x}Br_x$ solar cells fabricated with varying MABr concentrations are summarized in Table 6. The device incorporating 20 mg mL^{-1} MABr achieved the highest efficiency, with I_{sc} = 21.38 mA cm^{-2}, V_{oc} = 0.99 V, FF = 60.95%, and PCE = 12.56 ± 0.04%. This improvement is attributed to the enhanced film crystallinity and compact morphology that facilitate efficient charge transport and minimize trap-assisted recombination. Increasing MABr concentration beyond 30 mg mL^{-1} led to a gradual decline in current density and fill factor, consistent with the structural data showing bromide-induced lattice distortion and halide segregation. As shown in Table 6 and Figure 9, the photovoltaic parameters confirm this trend, where the 20 mg mL^{-1} MABr devices exhibit the most uniform and stable performance compared to higher bromide concentrations. The decrease in PCE and I_{sc} at 40 – 50 mg mL^{-1} indicates that excessive bromide incorporation generates non-uniform grain growth and increased charge recombination centers, reducing carrier collection efficiency. These results are consistent with previous reports that moderate halide substitution enhances perovskite film quality and device reproducibility, while excessive bromide content destabilizes the perovskite phase under humid conditions (Hoke et al., 2015).

The Ostwald ripening (OR) mechanism is a thermodynamically driven process that minimizes the system's total surface energy by dissolving smaller, high-energy crystallites and redepositing the ions onto larger, lower-energy grains (Lin et al., 2021; Mahmud et al., 2017; Yang et al., 2016; Zhu et al., 2016). This process is governed by the difference in chemical potential between small and large crystals, described by the Gibbs–Thomson relation. During OR treatment in the $CH_3NH_3PbI_{3\text{-}x}Br_x$ system, the small perovskite grains dissolve into the CH_3NH_3Br solution and recrystallize as larger grains with lower interfacial energy. Increasing MABr concentration reduces the total Gibbs free energy ($\Delta G < 0$), promoting thermodynamically stable crystal growth and improved crystallinity up to the optimal 40 mg/mL concentration. However, excessive bromide (>40 mg/mL) induces supersaturation and lattice strain, leading to secondary nucleation and halide seg-

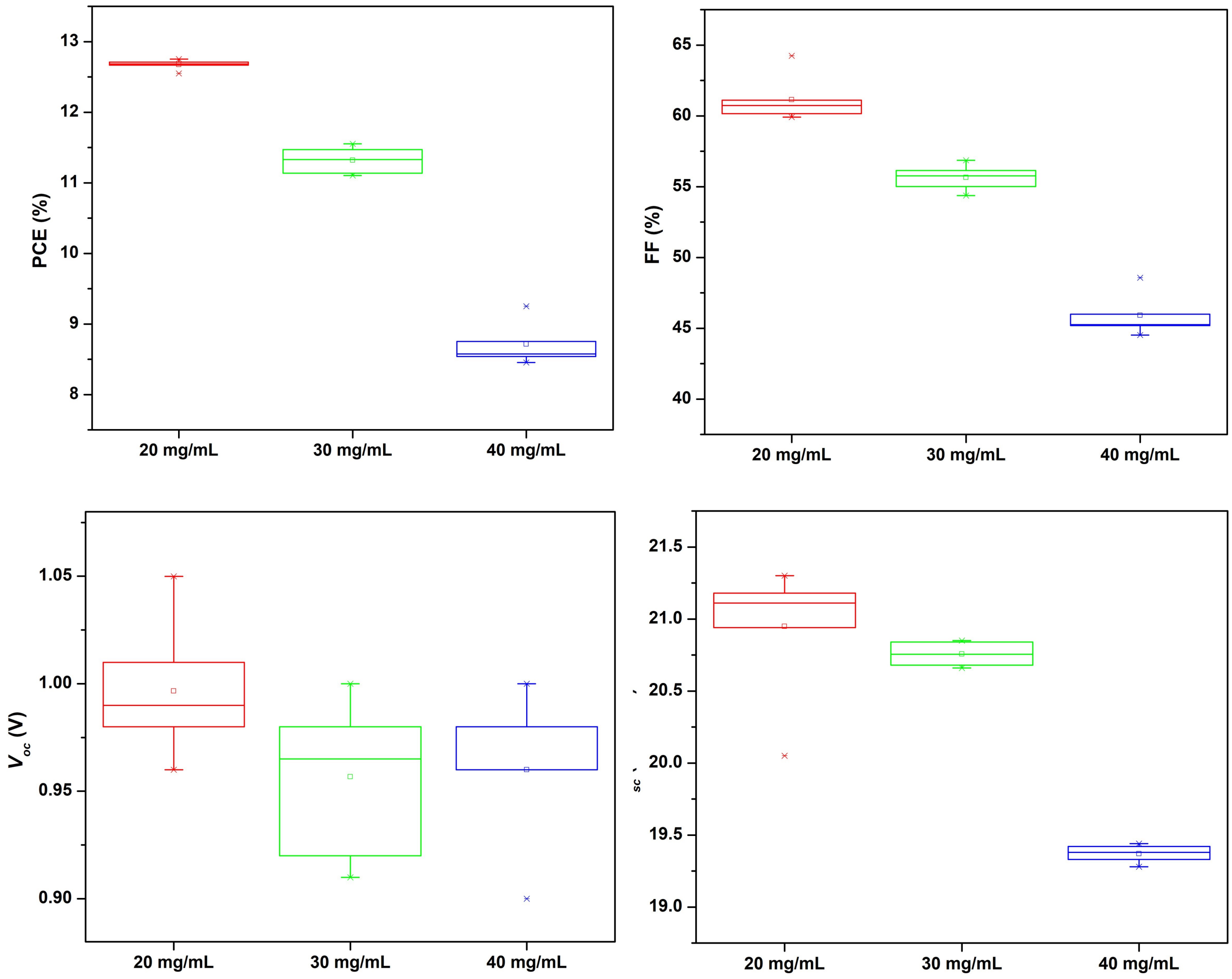

Figure 10. Statistics of PCE, FF, V_oc, and I_sc from Three Best Variation of MBr Concentration (20, 30, and 40 mg/mL). The Measurement was Conducted under Ambient Humidity, 1 Sun Illumination AM 1.5 Solar Light, 100 mW/cm^2, and at 58-60 °C.

regation, which elevate the system's free energy and reduce long-range crystallinity (Kim et al., 2016; Yang et al., 2020).

This thermodynamic behavior directly influences the correlation between grain size, crystallinity, and photovoltaic performance. Larger, well-oriented grains formed under moderate OR conditions reduce grain boundary density and defect states, facilitating efficient charge transport and minimizing trap-assisted recombination (Liu et al., 2020a; Zhu et al., 2016). Consequently, the perovskite film with 20-40 mg/mL MABr exhibits the highest carrier mobility and fill factor, yielding the optimal PCE of 12.56%. In contrast, excessive bromide incorporation (50 mg/mL) disrupts charge percolation pathways by introducing grain coarsening and phase segregation, which increase recombination losses and decrease photocurrent. The observed relationship follows a parabolic correlation model between crystallite size and device efficiency, where optimum energy conversion is achieved at intermediate grain size and highest orientation uniformity.

The reproducibility of perovskite solar cells based on prepared $CH_3NH_3PbI_{3\text{-}x}Br_x$, the solar cells performance was measured on 30 sample devices based on MABr concentration of 20, 30, and 40 mg/mL. Figure 10 presents the statistical distribution of the photovoltaic parameters (I_{sc}, V_{oc}, FF, and PCE) for CH_3NH_3 $PbI_{3\text{-}x}Br_x$ solar cells fabricated with different MABr concentrations (20, 30, and 40 mg/mL). The 20 mg/mL MABr-treated device exhibits the highest average performance with a PCE of approximately 12.5%, I_{sc} above 21 mA cm^{-2}, and FF exceeding 60%, indicating optimal halide incorporation and superior film uniformity. Increasing MABr concentration to 30 mg/mL leads to a slight reduction in all parameters, suggesting moderate bromide substitution introduces minor charge-transport resistance and grain-boundary recombination. At 40 mg/mL, the values of I_{sc}, FF, and PCE decrease significantly, reflecting reduced carrier extraction efficiency due to excessive bromide content and structural disorder, consistent with the SEM and XRD results. The relatively stable V_{oc} across all samples (0.97-1.00 V) indicates that bromide incorporation primarily affects charge transport rather than the energy alignment at interfaces. These statistical trends confirm that moderate bromide levels (≈20 mg/mL) provide the best balance between morphology, crystallinity, and photovoltaic performance under ambient humidity.

4. CONCLUSIONS

$CH_3NH_3PbI_{3-x}Br_x$ thin films were fabricated through an Ostwald ripening process with varied MABr concentrations to investigate the influence of bromide incorporation on structural and device performance. XRD characterization verified the formation of a tetragonal perovskite phase with progressive lattice contraction and enhanced (110) orientation up to 40 mg/mL MABr, confirming the substitution of I^- by Br^- within the crystal lattice. Surface and elemental analyses revealed that moderate bromide addition yielded compact, well-connected grains and uniform halide distribution, whereas excessive bromide resulted in grain coarsening, halide segregation, and morphological degradation under humid conditions. The optical results showed a tunable band gap associated with the degree of bromide incorporation, consistent with the observed structural modification. Among all compositions, the device with 20 mg/mL MABr achieved the best photovoltaic output (PCE = 12.56%), attributed to balanced crystallinity, reduced defect density, and efficient charge extraction. Overall, these results demonstrate that precise control of bromide content through Ostwald ripening is essential for optimizing film morphology, structural integrity, and stability of perovskite solar cells in humid environments.

5. ACKNOWLEDGEMENT

Financial support from National Research and Innovation Agency (BRIN) and Indonesia Endowment Fund for Education (LPDP), Ministry of Finance Republic of Indonesia through Research and Innovation for an Advanced of Indonesia (RIIM) Grant contract No. 59/IV/KS/05/2023 and T/9/UN-34.9/PT.01.03/2023 is gratefully acknowledged.

REFERENCES

Aftab, S., G. Koyyada, Z. Ali, M. A. Assiri, J. H. Kim, N. Rubab, and E. Akman (2025). Flexible Perovskite Solar Cells: A Revolutionary Approach for Wearable Electronics and Sensors. *Materials Today Energy*, **51**; 101872

Ahn, N., K. Kwak, M. S. Jang, H. Yoon, B. Y. Lee, J. K. Lee, P. V. Pikhitsa, J. Byun, and M. Choi (2016). Trapped Charge-Driven Degradation of Perovskite Solar Cells. *Nature Communications*, **7**(1); 13422

Al-janabi, A. A. H., R. Chtourou, T. B. Cedria, and H. Lif (2025). Mechanisms, Performance Enhancements, and Scalability Prospects of Solvent-Annealed Perovskite Solar Cells: A Review. *Journal of Applied Science and Nanotechnology (Assumed JASN)*, **5**(3); 39–59

Cahyorini, K., K. Suwardi, Indriana, and Narsito (2012). Synthesis and Characterization of Visible-Light Active Nitrogen-Doped TiO_2 Photocatalyst. *Asian Journal of Chemistry*, **24**(1); 255

Camizci, E., I. Dilci, Z. Xiao, and S. Sonmezoglu (2025). Defect Passivation and Crystallization Management Enabled by Thulium Dopant As B-Site Cation for Highly Stable and Efficiency Fully Inorganic Perovskite Solar Cells with Over 17% Efficiency. *Chemical Engineering Journal*, **512**; 162314

Catalán, J. and J. P. Catalán (2011). On the Solvatochromism of the $\pi \rightarrow \pi^*$ Electronic Transitions in Ketones. *Physical Chemistry Chemical Physics*, **13**(9); 4072–4082

Chen, B., S. Wang, Y. Song, C. Li, and F. Hao (2022). A Critical Review on the Moisture Stability of Halide Perovskite Films and Solar Cells. *Chemical Engineering Journal*, **430**; 132701

Chen, H. (2017). Two-Step Sequential Deposition of Organometal Halide Perovskite for Photovoltaic Application. *Advanced Functional Materials*, **27**(8); 1605654

Chen, W., Y. Wu, Y. Yue, J. Liu, W. Zhang, X. Yang, H. Chen, E. Bi, I. Ashraful, M. Grätzel, and L. Han (2015). Efficient and Stable Large-Area Perovskite Solar Cells with Inorganic Charge Extraction Layers. *Science*, **350**(6263); 944–948

Cheng, Y. and L. Ding (2021). Pushing Commercialization of Perovskite Solar Cells by Improving Their Intrinsic Stability. *Energy & Environmental Science*, **14**(6); 3233–3255

Elangovan, N. K., R. Kannadasan, M. F. Savio, S. Vinson Joshua, and M. Faheem (2024). The Influence of Methylammonium Iodide Concentration on the Properties of Perovskite Solar Cells. *Energy Science and Engineering*, **12**(5); 2004–2016

Farooq, U., M. Ishaq, U. A. Shah, S. Chen, Z. H. Zheng, M. Azam, Z. H. Su, R. Tang, P. Fan, Y. Bai, and G. X. Liang (2022). Bandgap Engineering of Lead-Free Ternary Halide Perovskites for Photovoltaics and beyond: Recent Progress and Future Prospects. *Nano Energy*, **92**; 106710

Fykouras, K., J. Lahnsteiner, N. Leupold, P. Tinnemans, R. Moos, F. Panzer, G. A. de Wijs, M. Bokdam, H. Grüninger, and A. P. M. Kentgens (2023). Disorder to Order: How Halide Mixing in $MAPbI_{3-x}Br_x$ Perovskites Restricts MA Dynamics. *Journal of Materials Chemistry A*, **11**(9); 4587–4597

Gan, Z., Z. Yu, M. Meng, W. Xia, and X. Zhang (2019). Hydration of Mixed Halide Perovskites Investigated by Fourier Transform Infrared Spectroscopy. *APL Materials*, **7**(3); 031107

Guo, P., J. Wang, X. Shen, Q. Lv, X. Li, Z. Xu, S. Han, Y. Bian, Y. Meng, L. Yang, C. Qin, K. M. Yu, J. C. Ho, and L. Xiao (2025). Bandgap Engineering of Halide Perovskite Nanoribbons for High-Performance Photodetection. *Nano Research*, **18**(5); 94907347

Hoke, E. T., D. J. Slotcavage, E. R. Dohner, A. R. Bowring, H. I. Karunadasa, and M. D. McGehee (2015). Reversible

Photo-Induced Trap Formation in Mixed-Halide Hybrid Perovskites for Photovoltaics. *Chemical Science*, **6**(1); 613–617

Huang, P. C., T. J. Yang, C. J. Lin, M. Y. Wang, and W. C. Lin (2024). Unraveling the Heat and UV-Induced Degradation of Mixed Halide Perovskite Thin Films via Surface Analysis Techniques. *Langmuir*, **40**(23); 11873–11887

Im, J. H., H. S. Kim, and N. G. Park (2014). Morphology-Photovoltaic Property Correlation in Perovskite Solar Cells: One-Step Versus Two-Step Deposition of $Ch_3NH_3PbI_3$. *Apl Materials*, **2**(8); 1–8

Jeon, N. J., J. H. Noh, Y. C. Kim, W. S. Yang, S. I. Ryu, and S. I. Seok (2014). Solvent Engineering for High-Performance Inorganic-Organic Hybrid Perovskite Solar Cells. *Nature Materials*, **13**(9); 897–903

Kim, G., N. Kwon, D. Lee, M. Kim, M. Kim, Y. Lee, W. Kim, D. Hyeon, B. Kim, M. S. Jeong, J. Hong, and J. Yang (2022). Methylammonium Compensation Effects in $MAPbI_3$ Perovskite Solar Cells for High-Quality Inorganic CuSCN Hole Transport Layers. *ACS Applied Materials & Interfaces*, **14**(4); 5203–5210

Kim, N., J. Ahn, M. Ko, S. Choi, W. Kim, W. Shin, S. Jung, H. Oh, M. Hwang, M. Ryu, and H. Lee (2024). Two-Step Preparation of Methylammonium Lead Triiodide Perovskite Film Via Electrospray Deposition of Methylammonium Iodide Solution for Solar Cell Applications. *Current Applied Physics*, **66**; 88–94

Kim, S. Y., H. J. Jo, S. J. Sung, and D. H. Kim (2016). Perspective: Understanding of Ripening Growth Model for Minimum Residual Pbi_2 and Its Limitation in the Planar Perovskite Solar Cells. *APL Materials*, **4**(10)

Kojima, A., K. Teshima, Y. Shirai, and T. Miyasaka (2009). Organometal Halide Perovskites as Visible-Light Sensitizers for Photovoltaic Cells. *Journal of the American Chemical Society*, **131**(17); 6050–6051

Kurniawidi, D. W., S. Rahayu, A. Budianto, K. Saputra, W. P. Agista, T. Suprayogi, and R. Marlina (2025). Synthesis and Characterization of $TiO_2/CaTiO_3$ Perovskite Composite Derived from *Pinctada maxima* Shell Waste. *Science and Technology Indonesia*, **10**(3); 924–942

Kusumawardani, C. and J. Ikhsan (2022). The Synthesis of Methylammonium Lead Iodide on Mesopore TiO_2 Thin Film Applying Ostwald Ripening Process under Ambient Condition. *Rasayan Journal of Chemistry*, **15**(3); 1678–1685

Li, J., Y. Yang, Z. Ye, D. Chen, J. Cui, and Q. Huang (2025). Controlled High-Quality Perovskite Single Crystals Growth for Radiation Detection: Nucleation and Growth Kinetics of Antisolvent Vapor-Assisted Crystallization. *Journal of Materials Science & Technology*, **232**; 276–282

Lin, Z., Y. Su, R. Dai, G. Liu, J. Yang, W. Sheng, Y. Zhong, L. Tan, and Y. Chen (2021). Ionic Liquid-Induced Ostwald Ripening Effect for Efficient and Stable Tin-Based Perovskite Solar Cells. *ACS Applied Materials & Interfaces*, **13**(13); 15420–15428

Liu, C., Y. B. Cheng, and Z. Ge (2020a). Understanding of Perovskite Crystal Growth and Film Formation in Scalable Deposition Processes. *Chemical Society Reviews*, **49**(6); 1653–1687

Liu, Z., L. Qiu, L. K. Ono, S. He, Z. Hu, M. Jiang, G. Tong, Z. Wu, Y. Jiang, D. Y. Son, Y. Dang, S. Kazaoui, and Y. Qi (2020b). A Holistic Approach to Interface Stabilization for Efficient Perovskite Solar Modules with Over 2,000-Hour Operational Stability. *Nature Energy*, **5**(8); 596–604

Mahmud, M. A., N. K. Elumalai, M. B. Upama, D. Wang, B. Puthen-Veettil, F. Haque, M. Wright, C. Xu, A. Pivrikas, and A. Uddin (2017). Controlled Ostwald Ripening Mediated Grain Growth for Smooth Perovskite Morphology and Enhanced Device Performance. *Solar Energy Materials and Solar Cells*, **167**; 87–101

Mehra, S., Mamta, J. Tawale, G. Gupta, V. N. Singh, A. K. Srivastava, and S. N. Sharma (2024). Evaluating Pb-based and Pb-free Halide Perovskites for Solar-Cell Applications: A Simulation Study. *Heliyon*, **10**(12); e33243

Ming, Y., Y. Cheng, W. Shen, H. Ran, J. Jiang, J. Wang, H. Qv, Y. Xue, Y. Zhao, J. Liu, Y. Tang, and S. Wang (2024). Crystallization and Defects Regulation of Efficient Perovskite Solar Cells via Surface Induced Secondary Grain Growth with Formamidine Iodine Treatment. *Journal of Alloys and Compounds*, **984**; 173913

Ngoc, H., N. Tran, W. Li, and X. Liu (2024). Perovskite Oxide Redox Materials for Two-Step Solar Thermochemical CO_2 Splitting. *Chemical Engineering Journal*, **500**; 156613

Nguyen, V. S., I. Zimmermann, E. Gré, K. Medjoubi, E. Bruhat, S. Berson, and J. Rousset (2023). Solvent-vapor Assisted Conversion Process for Hybrid Perovskites Coupling Thermal Evaporation and Slot-die Coating. *Materials Science in Semiconductor Processing*, **158**; 107358

Ogunniran, K. O. and N. T. Martins (2021). Humidity and Moisture Degradation of Perovskite Material in Solar Cells: Effects on Efficiency. In *IOP Conference Series: Earth and Environmental Science*, volume 655. IOP Publishing, page 012049

Sa, R., B. Luo, J. Huang, and D. Liu (2022). Bandgap Engineering and Optoelectronic Properties of All-inorganic Lead-free Pd-based Double Perovskites. *Arabian Journal of Chemistry*, **15**(5); 103785

Saptari, S. A., M. Mar'ah, Y. Taryana, and N. Sudrajat (2024). Synthesis and Characterization of Perovskite Manganate Based on $La_{0.7}Ca_{0.3}MnO_3$ with Ni and Ti Doping as Microwave Absorber Material. *Science and Technology Indonesia*, **9**(3); 577–585

Sinelnik, A. D., E. V. Bodyago, O. M. Kushchenko, I. I. Shishkin, N. K. Kuzmenko, and D. S. Gets (2024). Three-dimensional Perovskite-based Photonic Structures Made by Two-step Crystallization. *Optics and Laser Technology*, **170**; 110411

Sugiyarto, K. H., C. Kusumawardani, and K. E. Wulandari (2018). Synthesis and Structural Analysis of Powder Complex of Tris(Bipyridine)cobalt(II) Trifluoromethanesulfonate Octahydrate. *Indonesian Journal of Chemistry*, **18**(4);

696–701

Sutrisno, H., C. Kusumawardani, R. Y. Rananggana, and K. H. Sugiyarto (2018). Structural Analysis of Powder Tris (Phenanthroline) Nickel (II) Trifluoro Acetate. *Chiang Mai J. Sci*, **45**(7); 2768–2778

Taylor, A. D., Q. Sun, K. P. Goetz, Q. An, T. Schramm, Y. Hofstetter, M. Litterst, F. Paulus, and Y. Vaynzof (2021). A General Approach to High-efficiency Perovskite Solar Cells by Any Antisolvent. *Nature Communications*, **12**(1); 1878

Verma, A. and S. Jain (2024). Advances in Methylammonium Lead Halide Perovskites: Synthesis, Structural, Optical, and Photovoltaic Insights. *Oriental Journal of Chemistry*, **40**(4); 1056–1060

Vidyasagar, C. C., B. M. Muñoz Flores, and V. M. Jiménez Pérez (2018). Recent Advances in Synthesis and Properties of Hybrid Halide Perovskites for Photovoltaics. *Nano-Micro Letters*, **10**(4); 1–33

Wali, Q., I. E. Lee, T. C. Chuah, and R. Jose (2025). Overcoming the SnO_2 Bottleneck in Perovskite Solar Cells: Strategies for Enhancing Efficiency and Stability. *Materials Today Sustainability*, **32**; 101253

Watthage, S. C., Z. Song, G. K. Liyanage, A. B. Phillips, and M. J. Heben (2016). Investigation on the Nucleation and Growth Mechanisms of Perovskite Formation in the Two-Step Solution Process. In *2016 IEEE 43rd Photovoltaic Specialists Conference (PVSC)*. IEEE, pages 0831–0834

Wen, T., J. Zhou, J. Sun, Z. He, Y. Shi, C. Yu, M. Chen, Y. Wang, H. Zhong, S. Yang, Y. Hou, and Z. Yang (2025). Reducing Open-circuit Voltage Deficit of Wide-bandgap Perovskite Solar Cells by Heterocyclic Amine Modification. *Nano Energy*, **139**; 110954

Wozny, S., M. Yang, A. M. Nardes, C. C. Mercado, S. Ferrere, M. O. Reese, W. Zhou, and K. Zhu (2015). Controlled Humidity Study on the Formation of Higher Efficiency Formamidinium Lead Triiodide-Based Solar Cells. *Chemistry of Materials*, **27**(13); 4814–4820

Wu, T., Z. Qin, Y. Wang, Y. Wu, W. Chen, S. Zhang, M. Cai, S. Dai, J. Zhang, J. Liu, Z. Zhou, X. Liu, H. Segawa, H. Tan, Q. Tang, J. Fang, Y. Li, L. Ding, Z. Ning, Y. Qi, Y. Zhang, and L. Han (2021). The Main Progress of Perovskite Solar Cells in 2020-2021. *Nano-Micro Letters*, **13**(1); 152

Xing, G., N. Mathews, S. Sun, S. S. Lim, Y. M. Lam, M. Grätzel, S. Mhaisalkar, and T. C. Sum (2013). Long-Range Balanced Electron and Hole Transport Lengths in Organic-Inorganic $Ch_3nh_3pbi_3$. *Science*, **342**(6156); 344–347

Yang, M., T. Zhang, P. Schulz, Z. Li, G. Li, D. H. Kim, N. Guo, J. J. Berry, K. Zhu, and Y. Zhao (2016). Facile Fabrication of Large-Grain $CH_3NH_3PbI_{3\text{-}x}Br_x$ Films for High-Efficiency Solar Cells Via CH_3NH_3Br-Selective Ostwald Ripening. *Nature Communications*, **7**; 12305

Yang, Y., J. Wu, X. Wang, Q. Guo, X. Liu, W. Sun, Y. Wei, Y. Huang, Z. Lan, M. Huang, J. Lin, H. Chen, and Z. Wei (2020). Suppressing Vacancy Defects and Grain Boundaries via Ostwald Ripening for High-Performance and Stable Perovskite Solar Cells. *Advanced Materials*, **32**(7); 1904347

Yilmaz, O. and S. Yerci (2019). Fabrication of Mixed Halide Perovskite Films by Thermal Co-Evaporation. *Mugla Journal of Science and Technology*, **5**(2); 68–72

You, J., Y. M. Yang, Z. Hong, T. B. Song, L. Meng, Y. Liu, C. Jiang, H. Zhou, W. H. Chang, G. Li, and Y. Yang (2014). Moisture Assisted Perovskite Film Growth for High Performance Solar Cells. *Applied Physics Letters*, **105**(18)

Zhang, X., R. Chen, F. Dong, Y. Jiang, Y. Guo, N. Jia, L. Ma, Y. Zheng, Z. Liu, and H. Wang (2024). 1D-Phase-Induced Porous Templates for Efficient Two-Step-Processed Mixed-Halide Perovskite Solar Cells. *Chemical Engineering Journal*, **501**; 157647

Zhang, Y., Z. Fei, P. Gao, Y. Lee, F. F. Tirani, R. Scopelliti, Y. Feng, P. J. Dyson, and M. K. Nazeeruddin (2017). A Strategy to Produce High Efficiency, High Stability Perovskite Solar Cells Using Functionalized Ionic Liquid-Dopants. *Advanced Materials*, **29**(36); 1702157

Zhang, Y., X. Fu, Y. Su, and Y. Wu (2025a). Orientated Crystallization of $MAPbI_3$ Using Template Method for Efficient and Stable olar cells. *Materials Today Energy*, **49**; 101820

Zhang, Z., Y. Xu, S. Wang, C. Peng, P. Liu, S. Du, D. Pu, X. Zhao, M. Shang, G. Fang, and Z. Yu (2025b). Anti-Solvent Engineering for Efficient and Stable Perovskite Solar Cells with Preferentially Orientated 2-Dimensional/3-Dimensional Heterojunctions. *Energy & Environmental Science*, **18**(7); 3223–3234

Zhou, Y., O. S. Game, S. Pang, and N. P. Padture (2015). Microstructures of Organometal Trihalide Perovskites for Solar Cells: Their Evolution from Solutions and Characterization. *Journal of Physical Chemistry Letters*, **6**(23); 4827–4839

Zhu, W., C. Bao, Y. Wang, F. Li, X. Zhou, J. Yang, B. Lv, X. Wang, T. Yu, and Z. Zou (2016). Coarsening of One-Step Deposited Organolead Triiodide Perovskite Films Via Ostwald Ripening for High Efficiency Planar-Heterojunction Solar Cells. *Dalton Transactions*, **45**(18); 7856–7865